



Microstructure and microtexture evolution of dynamic recrystallization during hot deformation of a nickel-based superalloy



Mingjia Wang^{a,b}, Chaoyang Sun^{a,b,*}, M.W. Fu^{c,*}, Zhongli Liu^d, Chunhui Wang^{a,b}

^a School of Mechanical Engineering, University of Science and Technology Beijing, Beijing 100083, China

^b Beijing Key Laboratory of Lightweight Metal Forming, Beijing 100083, China

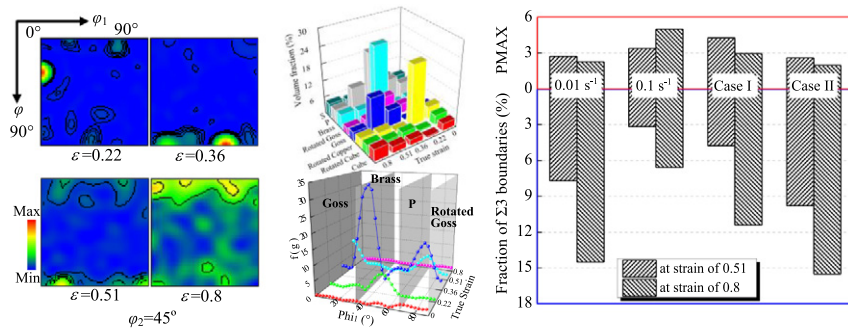
^c Department of Mechanical Engineering, The Hong Kong Polytechnic University, Hung Hom, Kowloon, Hong Kong, China

^d School of Nuclear Equipment and Nuclear Engineering, Yantai University, Yantai 264005, China

HIGHLIGHTS

- α -fiber in Euler space could be considered as the stable compression fiber texture.
- $\langle 101 \rangle$ and $\langle 001 \rangle$ poles were the compression and DRX crystallographic orientations.
- The new $\Sigma 3$ boundaries weakened the maximum pole density in the fully DRX processes.
- Cube-Twin components contributed partly to the formation of $\Sigma 3$ boundaries.

GRAPHICAL ABSTRACT



ARTICLE INFO

Article history:

Received 10 October 2019

Received in revised form 5 December 2019

Accepted 15 December 2019

Available online 17 December 2019

Keywords:

Microtexture evolution
Dynamic recrystallization
Nickel-based superalloy
Grain orientation
Hot deformation

ABSTRACT

Effect of strain rate route on the microstructure and microtexture evolution during the dynamic recrystallization (DRX) of a nickel-based superalloy subjected to the isothermal compression tests was investigated using electron back-scatter diffraction. The evolutions of microtexture components and fiber textures and the role of $\Sigma 3$ boundaries in microstructure on the pole density in the partially and fully DRX processes were explored. The α -fiber in Euler space is regarded as the compression microtexture. The locally organized substructures in the matrix grains are formed on certain $\{111\}$ slip planes with the high Schmid factor. Although the dislocation-free DRX grains show the random orientated distribution, the weak recrystallization $\langle 001 \rangle$ fiber parallel to the compression axis (ND) is developed at the high strain in the fully DRX processes. Whereas the compression $\langle 101 \rangle$ fiber parallel to ND in the partially DRX processes is sharpened. Moreover, the instantaneous decrease of strain rate leads to the highest fraction of $\Sigma 3$ grain boundaries, indicating the lowest pole density. Cube-Twin component adjacent to Cube component contributes partly to the formation of $\Sigma 3$ grain boundaries. The findings provide insights into the microtexture characteristics and enhance the understanding of the orientation dependence of the mechanical behavior of nickel-based superalloys.

© 2019 The Authors. Published by Elsevier Ltd. This is an open access article under the CC BY-NC-ND license (<http://creativecommons.org/licenses/by-nc-nd/4.0/>).

1. Introduction

The face-centered cubic (fcc) nickel-based superalloys exhibit superior microstructural stability, corrosion resistance, strength and creep

* Corresponding authors.

E-mail addresses: suncy@ustb.edu.cn (C. Sun), mmmwfu@polyu.edu.hk (M.W. Fu).

properties at high temperature, therefore, they are widely used for making the structures applied to the prolonged exposure in an aggressive environment at elevated temperature [1,2]. It is well known that most high-temperature structures are formed by hot working processes such as extrusion and forging, etc. The dynamic recrystallization (DRX) during the hot deformation of nickel-based superalloys is a major softening mechanism [3–5], and generates a large number of finer dislocation-free grains in the originally coarse grained structure. Furthermore, the directionality of properties is largely dependent on the microtexture formed in the finished product, since the preferred orientation of the newly formed grains is an inevitable behavior during deformation. Up to now, the study on the DRX process of the nickel-based superalloys has mainly focused on DRX nucleation mechanism and microstructure evolution, including the evolution characteristics of DRX volume fraction and grain size. Therefore, it is necessary to extensively study the characteristics of microtexture evolution during DRX of nickel-based superalloy.

In tandem with this research aspect, many prior researches have been done to explore the texture evolution in deformation and annealing of other fcc materials [6–9]. It is known that a combination of Brass and Goss components can be considered as the deformation textures in the fcc materials with low stacking fault energy (SFE). However, not much attention has been paid to the texture evolution characteristic in DRX process, especially for nickel-based superalloys. The generation of new grains and the strain hardening deformation of initial grains occur simultaneously during DRX, indicating the formation and evolution of microtexture being a more complex process. To address this issue, Xie et al. [10] has recently proven that the maximum pole density of an as-cast nickel-based superalloy in the uniaxial compression process was reduced with the increase of strain. Kumar et al. [11], Konkova et al. [12] and Jaladurgam et al. [13] revealed the formation of fiber textures after compression in the nickel-based superalloys based on the analysis of inverse pole figure. However, there is no consensus on the type of fiber textures during hot deformation in the above works. In addition, Buckingham et al. [14] showed the Rotated Cube component on the surface of sample and the Goss and Cube components located at the center of sample during the hot forging of an experimental V207M superalloy. The properties of metallic material, such as deformation behavior, strength and stress corrosion resistance, are tightly dependent on the texture change caused by different DRX degrees in microstructure. Although the limited explorations and researches have been conducted, there is a lack of qualitative and quantitative analysis of the microtexture formation and evolution of nickel-based superalloys. Furthermore, the factors affecting the change of maximum pole density (PMAX) in the DRX process of nickel-based superalloys also need to be further explored and identified.

Exploring and evaluating the physical process of microtexture modification is helpful for tailoring the mechanical properties of nickel-based alloys. In the present work, the evolution characteristics of microstructure and microtexture in different DRX processes resulted from the variation of strain rate were investigated using the electron back-scatter diffraction (EBSD). The evolution of microtexture components and the substructure characteristics of the dominant orientation grains during the full DRX process were studied. Moreover, the variation of PMAX with the conditions of the constant strain rate and the transient deformation caused by the momentary change of strain rate was also extensively analyzed, with the focus on revelation of the probable reason for the change of PMAX.

2. Experimental procedure

The nominal chemical composition (wt%) of the studied nickel-based superalloy is 0.03C–0.5Mo–0.5Si–0.3Mn–20Co–0.9Al–25Cr–0.7Fe–1.8Ti–2.0Nb and (Bal.) Ni. The specimens with 12 mm height and 8 mm diameter were taken from the forged billet. These specimens were heated to 1150 °C and held for 30 min, and subsequently

quenched in water. The isothermal uniaxial compression tests were then performed using a Gleeble 3500 thermo-mechanical simulator. A constant deformation temperature accompanied by the variations of true strain and strain rate during hot deformation was employed for the DRX process of the studied nickel-based superalloy. The imposed strain rate routes are illustrated in Fig. 1. The specific deformation conditions shown in Fig. 1(a) are the deformation temperature of 1100 °C, and two strain rates of 0.01 s⁻¹ and 0.1 s⁻¹ as well as four true strains of 0.22, 0.36, 0.51 and 0.8. Moreover, the transient deformation caused by the instantaneous change in strain rate was also implemented and was divided into the two cases shown in Fig. 1(b). Case I referred to scenario that the strain rate of 0.01 s⁻¹ was applied before the true strain of 0.36, and then the strain rate of 0.1 s⁻¹ was performed after the strain of 0.36. On the contrary, the specimen with the strain rate of 0.1 s⁻¹ was deformed to the true strain of 0.36, and then the subsequent strain rate was reduced to 0.01 s⁻¹ in Case II. In the two cases, the specimens were deformed to the true strain of 0.51 and 0.8, respectively. The microstructures of these two strains were observed.

Upon compression, the specimens were rapidly quenched in water to freeze their high temperature microstructures. The place selected for analysis of the microstructure characteristic was located at the central maximum deformation zone of the deformed specimen along the compression axis, involving the normal direction (ND, equivalent to compression direction) and the extension direction (ED). The observation surfaces of these specimens were polished mechanically and then electropolished in an electrolyte of 40 ml vitriol and 160 ml methyl alcohol for EBSD analysis. The area >1 mm² was scanned to give a reliably statistical explanation for microtexture. A Gaussian half-width of 5° and the harmonic series expansion method ($L = 22$, L is the truncation error) were used for calculating the orientation distribution functions (ODF) in order to evaluate the microtexture properly. In calculation of the volume fraction of a main component, a specific grain orientation was permitted within a 15° deviation from the ideal component unless otherwise indicated [15]. The aforementioned process was performed through the software Channel 5.

3. Results and discussion

3.1. True stress-strain curves

Fig. 2 shows the true stress-strain curves at different strain rate routes. The curves at the constant strain rate of 0.01 and 0.1 s⁻¹ show the characteristics of a single peak. Before peak stress (σ_p), the stress is increased due to the dislocation multiplication caused by strain hardening. While after σ_p , the stress is continuously decreased due to the dynamic softening dominated by DRX. After the transient deformation, the secondary hardening appears on the curve in Case I. The true stress is reduced again due to the ruling role of DRX after σ_p . It is remarkable that σ_p after the transient deformation in Case I is lower than that at the constant strain rate of 0.1 s⁻¹. The difference ($\Delta\sigma_p$) between the two σ_p values is about 30.60 MPa. It is because the stored dislocations at the low strain rate make a positive contribution to initiating DRX at the high strain rate in Case I, resulting in the difference. On the other hand, the true stress in Case II after the transient deformation is decreased rapidly, since the dislocation accumulation at the high strain rate is sufficient for the instantaneous occurrence of DRX at the low strain rate. Moreover, the true stress of the constant strain rate of 0.01 s⁻¹ and the Case II present a good reproducibility at the true strain of 0.8 and reach a steady state. Therefore, the deformation condition with the constant strain rate of 0.01 s⁻¹ is used to illustrate the following microtexture component evolution in the fully DRX process.

3.2. Evolution of microtexture components

The heat-treated specimen is defined as the initial material. The initial microstructure consisted of the nearly equiaxed, static

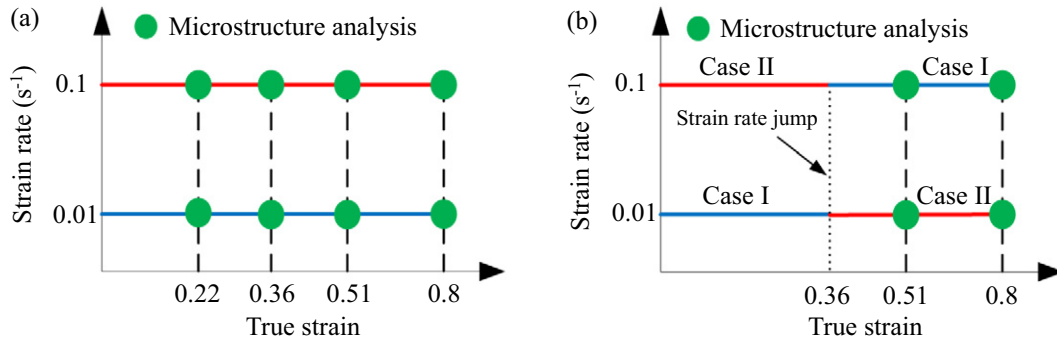


Fig. 1. Schematic of the variation of the strain rate at 1100 °C: (a) constant strain rate and (b) transient deformation.

recrystallization (SRX) grains and plentiful annealing twins is demonstrated in Fig. 3(a). The volume fraction of SRX grains (yellow) reaches 93.6%. Since the nucleation and uniform growth of SRX grains are characterized by the randomized orientation at grain boundaries during heat treatment [16], the $\{111\}$, $\{110\}$ and $\{100\}$ pole figures of the initial material in Fig. 3(b) display a weak texture prior to hot deformation.

Fig. 4 shows that the quantitative description of the microtexture evolution is presented by the sections ($\varphi_2 = 45^\circ$ and 65°) of ODFs at the strain rate of 0.01 s^{-1} and different true strains. The some ideal texture components are found to form during hot deformation of the nickel-based superalloy, including Rotated Copper $\{112\} \langle 110 \rangle$, Brass $\{110\} \langle 112 \rangle$, Rotated Goss $\{110\} \langle 110 \rangle$, Goss $\{110\} \langle 100 \rangle$, Rotated Cube $\{001\} \langle 110 \rangle$, Cube $\{001\} \langle 100 \rangle$, S $\{123\} \langle 634 \rangle$ [17] and P $\{110\} \langle 122 \rangle$ [18].

The evolution characteristic of maximum intensity of all the microtexture components and DRX volume fraction at 0.01 s^{-1} and different strains is plotted in Fig. 5. The overall maximum intensity displays an increased firstly and then decreased tendency with the increase of DRX fraction. This implies that the level of DRX volume fraction plays an observable role in the weakening of the maximum intensities at the high strain of all the microtexture components in the nickel-based superalloy. Under a lower strain, the leading role of deformed original grains in the microstructure makes the non-recrystallized (strain-hardened) grains rotate towards the one or some stable deformation textures during hot deformation [19]. Thus, the maximum intensity of all components is increased when the strain is less than 0.36. As the strain is further increased, more DRX grains formed by the bulging of original grain boundaries in the nickel-based superalloy are going to inherit the diverse misorientation of the neighboring initial grains and rotate to match with the preferred slip systems [20]. Eventually, the DRX grains tend to be the random oriented

characteristic, which in turn reduces the intensity of microtexture components.

Fig. 6 demonstrates the volume fractions corresponding to all the main microtextures derived from Fig. 4 under different strains. The fully SRX initial microstructure displays a rather weak microtexture with a random distribution. As the strain is increased, the microtexture is gradually transformed from the initial random components to some fcc ideal textures. When the strain is lower, the central region of the specimen is subjected to unidirectional compressive stress during isothermal compression process. Since the $\langle 110 \rangle$ direction is orientated to the shear direction in the fcc materials, the $\{hkl\} \langle 110 \rangle$ texture is the preferred texture component [21]. Therefore, the volume fraction of the typical shear component, such as Rotated Copper, is very high, and reaches 21.9% at the strain of 0.22. When the strain is 0.36, the stress in the central region is a state of triaxial compressive stress due to the obvious bulging of specimen caused by the effect of the friction between specimen and die, resulting in the smaller shear stress and thus weakening the effect of the shear texture component. Hence the unexpected Rotated Copper texture transforms into α -fiber texture characterized by the $\{110\} \langle uvw \rangle$ textures containing Goss, Rotated Goss, Brass and P, etc. Meanwhile, Goss component can run to P component by means of Brass component, resulting in the content variation of α -fiber texture [22]. Therefore, the volume fractions involving α -fiber texture increase in different degrees at the strain of 0.36. It is noted that the fraction of Goss, which is also considered as a recrystallization texture component, is increased until the true strain of 0.51. It is proven that a considerable degree of DRX has occurred at the strain of 0.51. A complete DRX microstructure is obtained when the strain is increased to 0.8. At this moment, the fractions of all the main microtextures are visibly small or up to the average. Therefore, when the microstructure is filled with DRX grains, there is reason to believe the maximum intensity of all the deformation textures is greatly decreased, as illustrated in Fig. 5. In addition, during hot deformation, the fractions of Rotated Cube and Cube components have a little bit increase, while that of S component is decreased firstly and then increased. However, the above three components vary within a little range.

The fiber texture plots which are related to the ideal textures in Euler space, as shown in Fig. 4, distinctly illustrate that the γ -fiber intensity involved in the fcc material is very weak. Therefore, Fig. 7 describes the variations of microtexture intensity ($f(g)$) along α -fiber, β -fiber and τ -fiber for comparing quantitatively the microtexture evolution in the DRX process. Fig. 7(a) reveals that the α -fiber ($\langle 110 \rangle // \text{ND}$ orientations, at $\varphi_2 = 0^\circ$, $\Phi = 45^\circ$, $\varphi_1 = 0^\circ$ to 90° in Euler space) shows an increasing firstly and then decreasing trend in the microtexture intensities along this fiber with the increasing deformation. It is clear that the high intensities along the fiber corresponding Brass (32.7) and P (15.2) texture components at the strain of 0.36. The strengthening Brass component during deformation process is typical characteristic in fcc materials with low SFE [23]. With the increasing strain, the intensity of α -fiber is decreased sharply. Eventually, when the strain is 0.8, there

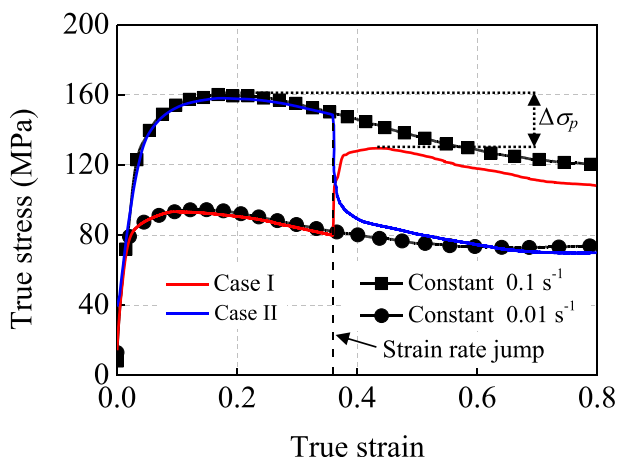


Fig. 2. True stress-strain curves under the variation of the strain rate.

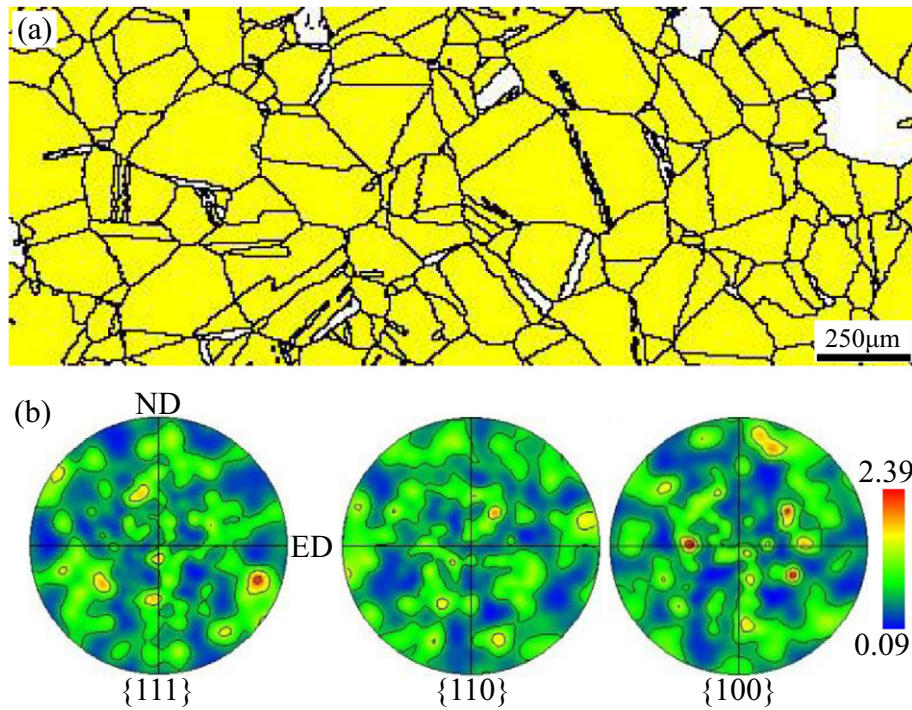


Fig. 3. The typical characteristic of the initial material expressed by (a) the microstructure (yellow corresponding to SRX grains) and (b) $\{111\}$, $\{110\}$ and $\{100\}$ pole figures.

is a little difference from the initial material. Fig. 7(b) shows the β -fiber (tilted 60° from ND towards ED) related to Copper, S and Brass orientations across φ_2 section. It is evident that the intensity of Copper component is weak, meanwhile, and that of S peaks at the strain of 0.36. The reorientation path of Copper to Goss orientations depending on mechanical twins is manifested by τ -fiber ($\{110\}$ //ED orientations, at $\varphi_2 = 45^\circ$, $\varphi_1 = 90^\circ$, $\Phi = 0^\circ$ to 90° in Euler space) in low SFE materials [24]. The intensity variations of different microtexture components along the τ -fiber are described in Fig. 7(c). The intensities corresponding to Copper and Copper-Twin orientations are relative low and have a little difference at any given stage of deformation. The intensity of Goss component is the most significant at the strain of 0.51.

3.3. Characteristic of the dominant orientation grains

The mechanical twinning and dislocation slip are two basic mechanisms for the plastic deformation of metallic materials. The prevailing one of these two mechanisms is mainly dependent on the SFE of metallic material and deformation conditions (i.e., temperature, strain rate and strain). No evidence of mechanical twins is observed in Figs. 4 and 7(c), indicating that the deformation is accommodated entirely by slip. The plastic deformation results in the orientation difference within the randomly orientated matrix grain, which can generate geometrically necessary dislocation (GND) to accommodate the intragranular orientation gradient [25]. The four matrix orientation grains with the

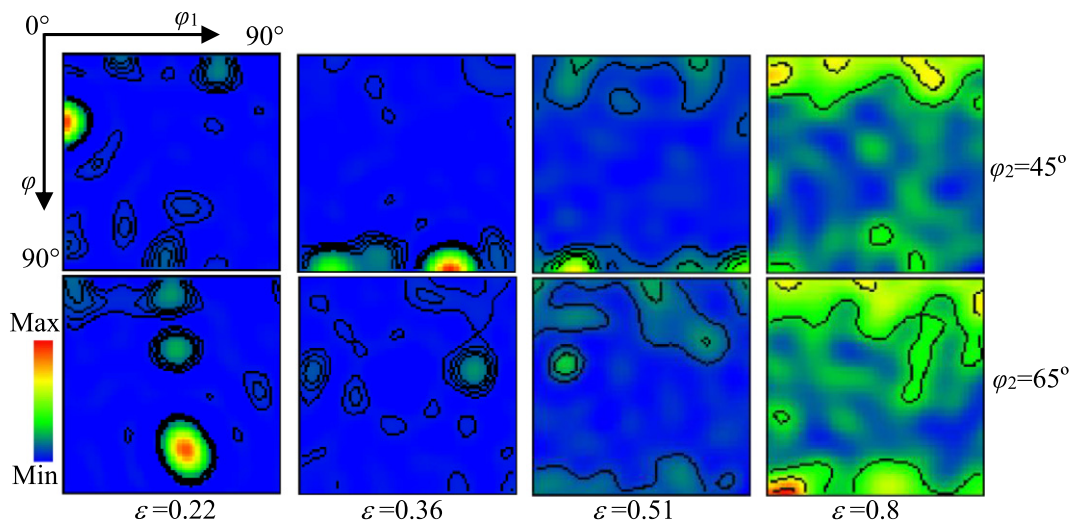


Fig. 4. The $\varphi_2 = 45^\circ$ and 65° sections of ODF under the deformation conditions of different true strains and the strain rate of 0.01 s^{-1} .

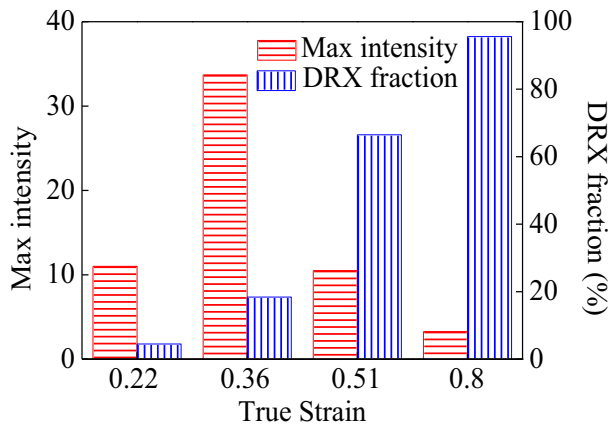


Fig. 5. Relationship between the maximum intensity of the ideal components and the volume fraction of DRX under the deformation condition of different true strains and the strain rate of 0.01 s^{-1} .

dominant volume fraction in Fig. 6 are emphatically analyzed, as shown in Fig. 8(a). The true strains corresponding to Rotated Copper, P, Brass and Goss orientation grains are 0.22, 0.36, 0.36, and 0.51, respectively. Based on the Schmid factors (summarized in Table 1) of slip systems and their grain orientations, the traces of $\{111\}$ slip planes are delineated. The CD letters denote the co-directional slip systems [26], and the black arrow in the crystal lattice indicates the ND of the preferred orientation grain. The accumulation of GND leads to the low angle grain boundaries (3° – 15°) in individual grains. Moreover, the local mobility differences of grain boundaries seem to further complicate the observed substructure in these grains due to the arrays of GND walls [27]. It is found that the some GND walls appear to be parallel to certain $\{111\}$ slip planes in Rotated Copper, P, Brass and Goss orientation grains. For example, the partial GND walls in Rotated Copper grain are parallel to (111) and $(1-11)$ planes, and the partial walls in P grain are parallel to (111) plane, as well as the partial walls in Brass and Goss grains are parallel to $(1-11)$ plane. Therefore, it can be concluded that the locally organized substructure is formed on $\{111\}$ slip planes with the value of high Schmid factor, meanwhile, the multiple slip systems are activated within these grains. Fig. 8(b) demonstrates the distribution of local misorientation between neighboring pixels in these orientation grains. The distribution for these grains is shifted to the higher values (the average

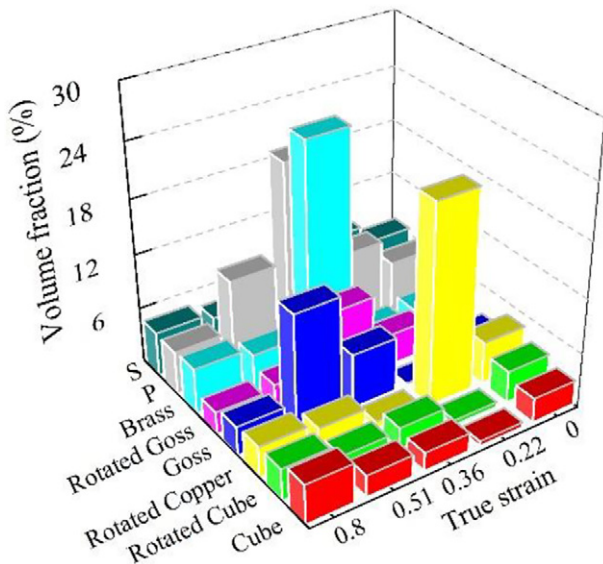


Fig. 6. The volume fraction of the main microtexture components at the strain rate of 0.01 s^{-1} .

angle θ_{AVE}) with the increase of strain, indicating the occurrence of slip [24].

Further insights into the misorientation gradient of the dominant orientation grains during DRX process, the point to origin (cumulative) and point to point (local) misorientations are quantified and depicted in Fig. 9, respectively. The cumulative misorientations within these deformed matrix orientation grains show the rather higher misorientation gradient (exceeding 10° , blue dashed line) as plotted in Fig. 9(a)–(d). It clearly indicates the active dislocation multiplication/rearrangement process. This is due to the above multiple slip systems running concurrently in these grains, and the running can promote the appearance of the intricate but locally organized substructure formed by dislocation walls (or microbands) in Fig. 8(a). However, Fig. 9(e)–(h) reveal that the maximum cumulative misorientations tend to be obviously weakened in the dominant orientation DRX grains. This phenomenon is characterized by a significant decrease in peak cumulative misorientation (not exceeding 1.5°). The lowering cumulative misorientation is caused by the substructure evolution [28], such as dislocation motion and lattice rotation, showing the random orientation characteristic of the dislocation-free DRX grains. Furthermore, the local misorientation gradient is quite weak especially within the DRX orientation grains. The deformation time caused by the low strain rate (0.01 s^{-1}) is sufficient so that the dynamics involved in the substructure evolution and dislocation rearrangement are raised to preclude the formation of the high intragranular local misorientation gradient.

3.4. Microstructure and crystallographic orientation

The deformation microstructures and crystallographic orientations of different strain rates are shown through the grain boundary maps and inverse pole figures (IPFs) parallel to ND, respectively, as illustrated in Figs. 10 and 11. The red and black lines in the microstructures denote the annealing $\Sigma 3$ twin boundaries and the grain boundaries with the misorientation angle $>15^\circ$, respectively. Obviously, the changes in strain and strain rate affect the microstructure, fiber orientation and pole density. From Fig. 2, the peak strains corresponding to the values of σ_p at the strain rate of 0.01 and 0.1 s^{-1} are less than 0.22, indicating the occurrence of DRX at the strain of 0.22. When the strain is increased, the volume fraction of DRX in Fig. 10 is also gradually increased, while this fraction of each true strain at 0.01 s^{-1} is higher than that at 0.1 s^{-1} . Furthermore, from Fig. 10(a), the compression fiber at the strain of 0.22 shows no particular dominant orientation along ND. When the true strains are increased to 0.36 and 0.51, $\langle 101 \rangle$ fiber appears. A considerable amount of initial deformed (strain-hardened) grains is still in the microstructures with the strains of 0.36 and 0.51, resulting in the compression orientations near to $\langle 101 \rangle$ fiber. Therefore, under these two true strains, the highlighting of $\langle 101 \rangle$ fiber texture is due to the presence of the abundant strain-hardened grains [29]. The $\langle 001 \rangle$ fiber is sharpened when the strain is increased to 0.8. Although the analysis of above sections indicates that the DRX grains with dislocation-free present the characteristic of random orientation distribution, the fiber orientation can be rotated from $\langle 101 \rangle$ to $\langle 001 \rangle$, when the DRX grains are filled with the microstructure with the strain of 0.8. In other words, the $\langle 001 \rangle$ fiber in this nickel-based superalloy is considered as the crystallographic orientation caused by the DRX grains. Moreover, the variation tendency of PMAXs given by IPFs in Fig. 10(a) is similar to the maximum intensity of the ideal microtexture components shown in Fig. 5. However, a large proportions of deformed matrix grains in the microstructures of different strains at 0.1 s^{-1} are subjected to be strain-hardened certainly during hot deformation [30], resulting in PMAX in Fig. 10(b) being continuously increased with strain. Meanwhile, the $\langle 101 \rangle$ fiber in Fig. 10(b) induced by the development of the strain-hardened structure at the high strain rate are gradually intensified. With the increase of strain, the increase of PMAX near to $\langle 101 \rangle$ fiber as a compression microtexture has also been reported in pure nickel and pure copper materials [31]. Thus, in the nickel-based superalloy, the crystallographic

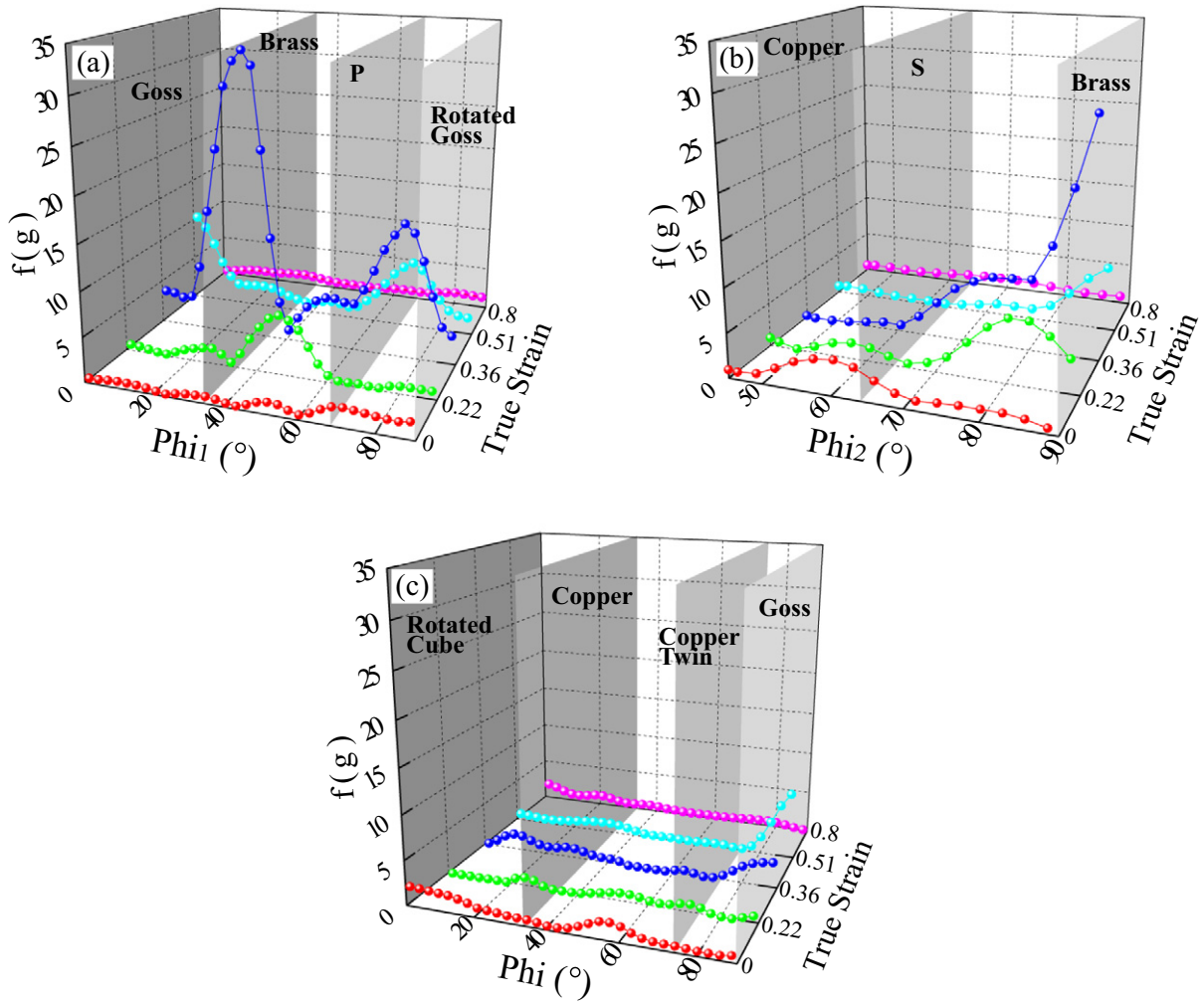


Fig. 7. Microtexture intensity distribution of the nickel-based superalloy at the strain rate of 0.01 s^{-1} in a fiber representation of Euler space: (a) α -fiber, (b) β -fiber and (c) τ -fiber.

orientation parallel to ND tends to form the $\langle 101 \rangle$ fiber highlighted by the deformed matrix grains, while those orientations dominated by the DRX grains are a tendency towards $\langle 001 \rangle$ fiber. On the other hand, by comparing Fig. 10(a) and (b), it is found that PMAXs at 0.1 s^{-1} are greater than PMAXs at 0.01 s^{-1} under the higher strain (0.51 and 0.8)

condition. This phenomenon is similar to other fcc materials [19,32]. The low strain rate is more conducive to the DRX occurrence at a constant temperature. The DRX grains show the rather random orientation and thereby weaken the microtexture intensity, as the above analysis in the previous sections.

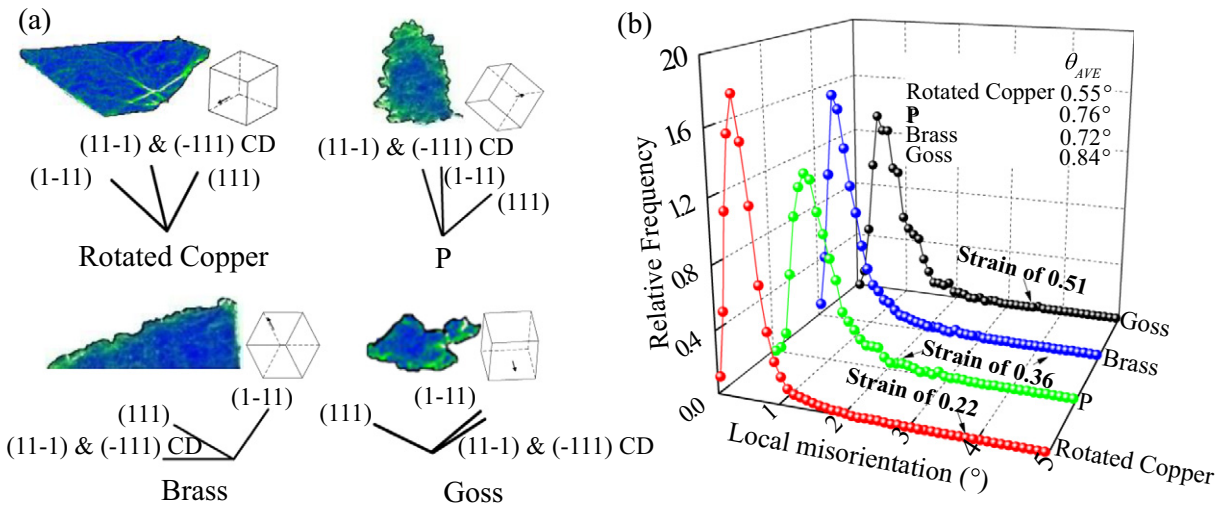


Fig. 8. (a) GND distributions and the traces of active $\{111\}$ slip planes in the dominant Rotated Copper, P, Brass and Goss orientation grains and (b) the distributions of local misorientation in these grains. The black and white lines in (a) denote the boundary misorientation angle with $>15^\circ$ and $3^\circ\text{--}15^\circ$, respectively.

Table 1

Schmid factor values for {111}⟨110⟩ slip systems of the dominant ideal orientation grains: Rotated Copper, P, Brass and Goss.

Plane	(111)			(11-1)			(-111)			(1-11)		
	[01-1]	[10-1]	[1-10]	[011]	[101]	[1-10]	[01-1]	[101]	[110]	[011]	[10-1]	[110]
Rotated Copper	0.17	0.10	0.07	0.34	0.15	0.01	0.06	0.31	0.24	0.37	0.05	0.32
P	0.43	0.31	0.01	0.05	0.06	0	0.17	0.32	0.25	0.42	0.17	0.26
Brass	0.06	0.01	0.05	0.24	0.26	0.02	0.02	0.26	0.25	0.32	0	0.31
Goss	0.38	0.09	0.29	0.01	0.02	0	0.08	0.18	0.10	0.47	0.07	0.39

Fig. 11 shows the microstructures and crystallographic orientations at the higher strain after the transient deformation. Obviously, the microstructures after the transient deformation show that the DRX fractions at the instantaneously increased strain rate are less than that at the instantaneously decreased strain rate. The reason is that the higher strain rate before the transient deformation accumulates the higher dislocation density for the nucleation of new grains, and the subsequent lower strain rate after transient deformation provides the adequate time for the development of new grains. Furthermore, a lot of the strain-hardened matrix grains in the microstructures at the strain of 0.51 show the crystallographic orientations near to the ⟨101⟩ fiber in Cases I and II. The dominant proportion of DRX grains in the microstructures at the strain of 0.8 in Cases I and II is apparent due to the increase of true strain, and the ⟨001⟩ fiber is formed consequently. Meanwhile, PMAXs in Cases I and II are decreased with the increase of strain, respectively.

The crystal plane normal and direction with the same indices in cubic crystals are paralleled, and thus the ND of specimen can be expressed in the form of crystal plane coordinate [33]. Therefore, when the strains are 0.36, 0.51 and 0.8, the compression and recrystallization fibers from Figs. 10 and 11 are in accordance with the {110} (corresponding to α -fiber) and {001} (corresponding to Rotated Cube and Cube components) plane microtextures from the $\varphi_2 = 45^\circ$ sections of ODF in Fig. 4, respectively. It indicates the consistency of microtexture evolution in the different DRX processes caused by the variation of strain rate in the nickel-based alloys.

3.5. Role of annealing twins

It is worth mentioning that when the strain is 0.8, the fractions of DRX grains in the microstructures at the constant 0.01 s^{-1} and Cases I and II are quite high, as shown in Figs. 10(a) and 11. However, a more or less difference among PMAXs under these conditions is demonstrated. The known fact is that due to the migration of grain boundaries with the misorientation angle $>15^\circ$ [34], the annealing twins can form during DRX of the materials with low SFE [35]. The fraction of the first-order twins ($\Sigma 3$) in other nickel-based superalloys is much more than that of other higher orders annealing twins during hot deformation [36,37]. Moreover, the $\Sigma 3$ boundaries are featured by 60° misorientation around (111) axis. Therefore, the formation of $\Sigma 3$ boundaries provides a significant way to understand the difference of crystallographic orientation, and thus gives a feasibility to analyze the change of PMAX in the studied nickel-based superalloy. The values of PMAX under the conditions of true strains of 0.51 and 0.8 in Figs. 10 and 11 are again given in Fig. 12(a) to compare the changing tendency of $\Sigma 3$ boundaries in Fig. 12(b). It is found that the fraction of $\Sigma 3$ boundaries in Fig. 12(b) under the testing conditions is increased with the true strain. It is attributed to the higher mobility of grain boundaries, the higher frequency of twinning. Moreover, Fig. 12 reveals that the greater fraction of $\Sigma 3$ boundaries corresponds to the smaller PMAX under all the deformation conditions, except for the strain rate of 0.1 s^{-1} . That is to say, the fraction of annealing twin boundaries in the microstructures where the DRX grains are absolutely dominant can cause a difference in the values

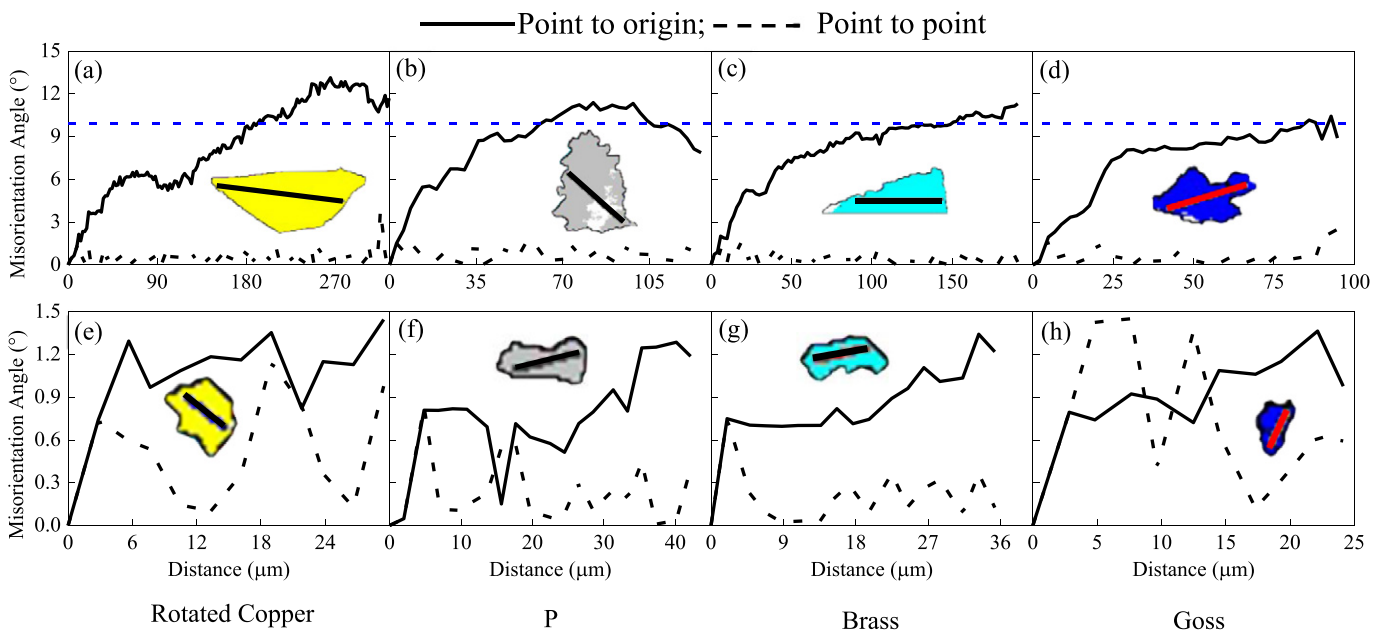


Fig. 9. Misorientation gradient scans along the lines in the dominant Rotated Copper, P, Brass and Goss orientation grains at the strain rate of 0.01 s^{-1} : (a)–(d) deformed matrix orientation grains; (e)–(h) DRX orientation grains.

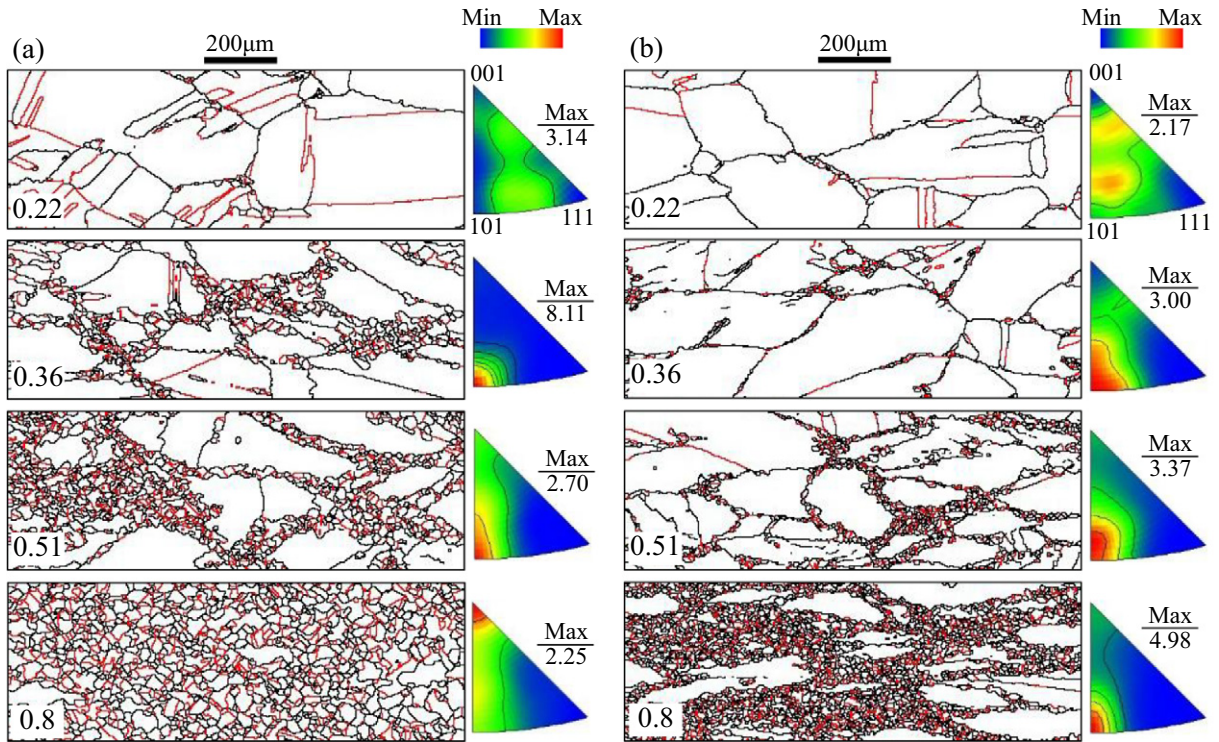


Fig. 10. Microstructure evolution and crystallographic orientations represented by IPFs/ND at the strain rate of (a) 0.01 s^{-1} and (b) 0.1 s^{-1} .

of P_{MAX}, as shown by the strain of 0.8 in Figs. 10(a) and 11. On the other hand, Fig. 12 also depicts that P_{MAX} and fraction of $\Sigma 3$ boundaries at 0.1 s^{-1} are increased with the true strain. The phenomenon roots in the fact that the twinning occurs within the DRX grains during hot deformation. From Fig. 10(b), the initial $\Sigma 3$ boundaries in the initial grains disappear gradually with the increase of strain, since the grain rotation causes the initial $\Sigma 3$ boundaries to lose the twin nature. Although the regenerative $\Sigma 3$ boundaries within the DRX grains are increased with strain, the new $\Sigma 3$ boundaries do not affect the development of the strain-hardened structure, resulting in the continuous increase of P_{MAX} with the true strain.

In order to understand the role of the regenerated annealing twins in the formation of recrystallization $\langle 001 \rangle // \text{ND}$ fiber and the decrease of P_{MAX} at the higher strains of 0.01 s^{-1} and Cases I and II, the enlarged microstructure and orientation characteristics obtained at the strain

rate of 0.01 s^{-1} and the strain of 0.51 are given in Fig. 13. It is reported that the twinning within Brass and Goss orientation grains facilitates the development of α -fiber components during SRX of fcc cold rolled and annealed high-entropy alloy and TWIP steel [38,39]. Fig. 13(a) exhibits the orientation distribution of some ideal microtexture components in the microstructure. The red and black lines are the $\Sigma 3$ boundaries and the grain boundaries with the misorientation angle $>15^\circ$, respectively. The colorful grains represent the four ideal orientation grains, while the white grains denote other random orientation grains. It is apparent that only a small number of $\Sigma 3$ boundaries are associated with Brass and Goss oriented grains, which indicates the twinning during DRX of the nickel-based alloy is different from that during SRX of other fcc materials. Furthermore, the annealing twin contributes to the final Cube recrystallization texture during DRX of an fcc austenitic stainless steel [40], however, the further explanation is missing. From Fig. 13(a),

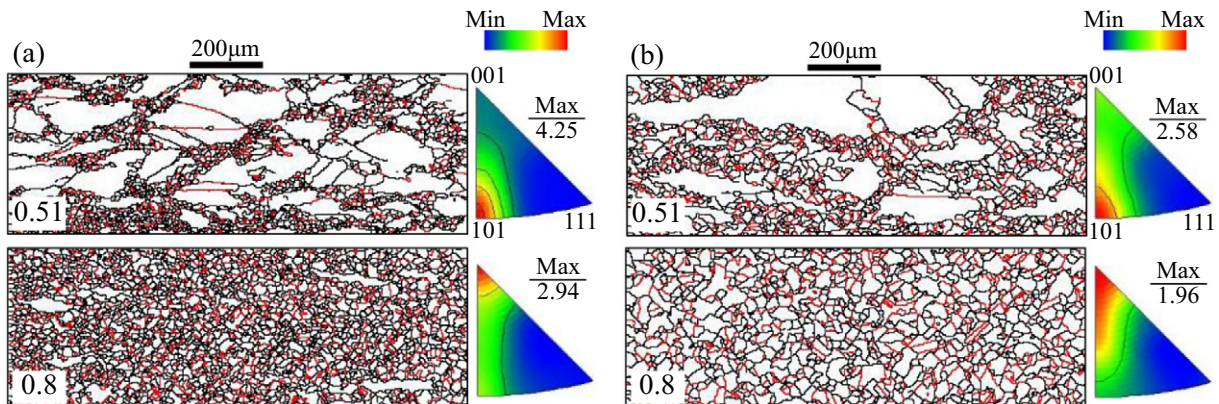


Fig. 11. The microstructure evolution and crystallographic orientations expressed by IPFs/ND after the transient deformation: (a) Case I and (b) Case II.

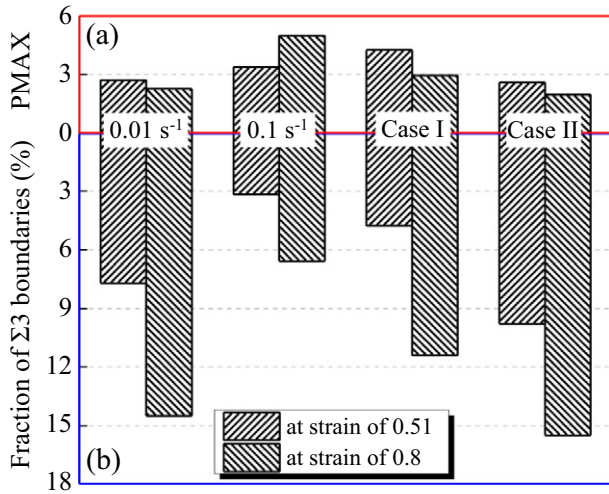


Fig. 12. Variations of (a) PMAX and (b) fractions of Σ3 boundaries at the true strain of 0.51 and 0.8 in Figs. 10 and 11.

some named Cube-Twin {212} <122> orientation grains are accompanied by the Cube grains. The IPF//ED in Fig. 13(b) demonstrates that the sharpened <122> pole is the evidence for the presence of Cube-Twin component. However, the <122> fiber with the lower PMAX renders a less significant performance in the 65° section of ODF with the strain of 0.51 in Fig. 4. Moreover, the positional relationship between Cube (Grain 1) and Cube-Twin (Grain 2) orientation grains in {111} pole figure is displayed in Fig. 13(c). A near-twin misorientation of grains is decided by Brandon criterion [41]. The misorientation relationship between Grains 1 and 2 in Fig. 13(c) show a 58.99° [1-1-1], which is much less than 15°/(Σ)^{1/2} = 8.66° obtained by the criterion of ideal Σ3 boundaries (60° <111>). Therefore, there is a precise Σ3 relationship

between Cube and Cube-Twin orientation grains. In addition, the fractions of Cube component and new Σ3 boundaries are increased with strain, as illustrated in Figs. 6 and 12(b). The interaction mechanism between the two components is predictable during DRX of the nickel-based superalloy. However, the fractions of Cube (4.3%) and Cube-Twin (3.42%) components are much less than that of Σ3 boundaries (14.5%) at the strain of 0.8 and 0.01 s⁻¹, since most of twinning occurs within the randomly oriented DRX grains from Fig. 13(a). Hence, the contribution of Cube-Twin component to the formation of Σ3 boundaries is not much, but its role cannot be ignored. Whereas Cube-Twin component contributes to Cube component involved in <001>//ND in the full DRX state. Moreover, according to Fig. 6, the fraction of Goss component is the largest at the strain 0.51. Rotated Cube component involved in the final recrystallization <001>fiber//ND can be concerned with a rotation of 35° <111> by Goss component [40].

The fraction of Σ3 boundaries increased to a certain degree can reduce PMAX during DRX of the nickel-based superalloy. The similar viewpoint was reported in the other fcc material [42]. The new twinning process occurs in the DRX grains. The annealing twins composed of stacking faults on the consecutive {111} plane can be explained by the growth accident model [43]. In this model, the growth accident happens on the propagating of {111} steps related to the migration of grain boundaries. The difference of dislocation densities across the grain boundary is regarded as the driving force for the migration of grain boundaries [44]. Moreover, the movement distance of grain boundaries is increased by the sufficient deformation time. Therefore, in this research, the instantaneous decrease of strain rate during hot deformation provides not only the high dislocation density, but also the sufficient time for the grain boundary migration, leading to the minimum of PMAX in Case II, as shown in Fig. 12(a). This also shows that the frequency of twinning is proportional to the fraction of DRX grains. Furthermore, although the highest dislocation density is produced by the constant strain rate of 0.1 s⁻¹, the insufficient deformation time causes the lowest twinning frequency and DRX fraction. This is not enough to

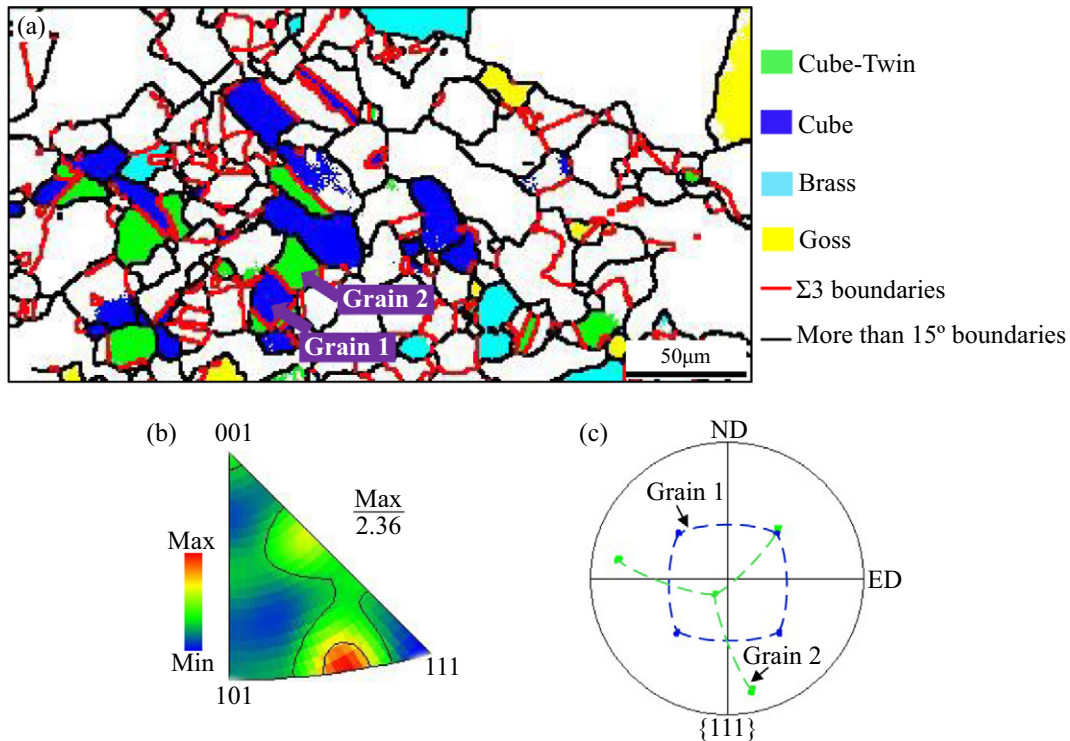


Fig. 13. Under the true strain of 0.51 and the strain rate of 0.01 s⁻¹: (a) the orientation distribution of ideal Brass, Cube and Cube-Twin components in microstructure, (b) the crystallographic orientation expressed by IPF//ED and (c) the positions of Cube and Cube-Twin orientation grains in {111} pole figure.

offset the development of strain-hardened grains, resulting in the continuous increase of P_{MAX} with strain, as illustrated in Fig. 10(b).

4. Conclusions

The microstructure and microtexture characteristics of a nickel-based superalloy in different DRX processes caused by the variation of strain rate were investigated. The major findings drawn from this work are summarized in the following:

- (1) The evolution path of microtexture components in the full DRX process with the constant low strain rate (0.01 s^{-1}) is as follows: a random distribution caused by SRX → Rotated Copper component with the high volume fraction → α -fiber microtexture with the highest intensity focused on Brass and P components → α -fiber microtexture centered on Goss component → a random distribution caused by DRX.
- (2) The plastic deformation under the testing conditions is accommodated entirely by slip. The partial dislocation walls in the dominant matrix orientation grains (i.e., Rotated Copper, P, Brass and Goss) tend to be formed on {111} slip planes with the high values of Schmid factor. Meanwhile, these grains show the similar locally organized substructures formed by the high misorientation gradient.
- (3) The $\langle 101 \rangle$ with the high P_{MAX} and $\langle 001 \rangle$ with the low P_{MAX} fibers are considered as the compressive and recrystallized crystallographic orientations parallel to ND, respectively. The high fraction of regenerative $\Sigma 3$ boundaries at the strain of 0.51 and 0.8 decreases the values of P_{MAX} under the strain rate of 0.01 s^{-1} and transient deformation. Nevertheless, the increase of $\Sigma 3$ boundaries at the high strain rate (0.1 s^{-1}) does not play a role in the continuous increase of P_{MAX} with strain due to the generation of $\Sigma 3$ boundaries within DRX grains.
- (4) The maximum mobility of grain boundaries caused by the instantaneous decrease of strain rate (Case II) during hot deformation maximizes the twinning frequency within the DRX grain, and thus minimizes the value of P_{MAX} in Case II. The generation of regenerated $\Sigma 3$ boundaries is basically concerned with the migration of grain boundaries, and is also partly affected by the evolution of Cube and Cube-Twin components.

CRediT authorship contribution statement

Mingjia Wang: Conceptualization, Investigation, Methodology, Data curation, Writing - original draft. **Chaoyang Sun:** Conceptualization, Validation, Methodology, Resources, Supervision, Funding acquisition, Writing - review & editing. **M.W. Fu:** Conceptualization, Methodology, Writing - review & editing. **Zhongli Liu:** Methodology, Investigation. **Chunhui Wang:** Methodology, Investigation.

Declaration of competing interest

The authors declare no potential conflict of interest or competing financial interest.

Acknowledgements

Authors acknowledge the funding supported by NSAF Joint Fund (No. U1730121), National Natural Science Foundation of China (No. 51575039), Beijing Municipal Natural Science Foundation (No. 3182025), Joint Foundation (general) project of the Ministry of Education of China (No. 6141A020221) and Fundamental Research Funds for the Central Universities (No. FRF-BD-19-003A and No. FRF-GF-19-003A).

Data availability

The raw data supporting the findings are available from the corresponding authors of this study.

References

- [1] A.J. Goodfellow, E.I. Galindo-Nava, C. Schwalbe, H.J. Stone, The role of composition on the extent of individual strengthening mechanisms in polycrystalline Ni-based superalloys, *Mater. Des.* 173 (2019), 107760.
- [2] T. Zhang, J. Jiang, B.A. Shollock, T.B. Britton, F.P.E. Dunne, Slip localization and fatigue crack nucleation near a non-metallic inclusion in polycrystalline nickel-based superalloy, *Mater. Sci. Eng. A* 641 (2015) 328–339.
- [3] X.M. Chen, Y.C. Lin, M.S. Chen, H.B. Li, D.X. Wen, J.L. Zhang, M. He, Microstructural evolution of a nickel-based superalloy during hot deformation, *Mater. Des.* 77 (2015) 41–49.
- [4] Z. Wan, L. Hu, Y. Sun, T. Wang, Z. Li, Hot deformation behavior and processing workability of a Ni-based alloy, *J. Alloys Compd.* 769 (2018) 367–375.
- [5] M. Wang, W. Wang, Z. Liu, C. Sun, L. Qian, Hot workability integrating processing and activation energy maps of Inconel 740 superalloy, *Mater. Today Commun.* 14 (2018) 188–198.
- [6] R. Jamaati, M.R. Toroghinejad, Effect of stacking fault energy on deformation texture development of nanostructured materials produced by the ARB process, *Mater. Sci. Eng. A* 598 (2014) 263–276.
- [7] C. Haase, L.A. Barrales-More, Influence of deformation and annealing twinning on the microstructure and texture evolution of face-centered cubic high-entropy alloys, *Acta Mater.* 150 (2018) 88–103.
- [8] R. Madhavan, R.K. Ray, S. Suwas, Texture transition in cold-rolled nickel-40 wt.% cobalt alloy, *Acta Mater.* 74 (2014) 151–164.
- [9] M. Klimova, S. Zherebtsov, N. Stepanov, G. Salishchev, C. Haase, D.A. Molodov, Microstructure and texture evolution of a high manganese TWIP steel during cryorolling, *Mater. Charact.* 132 (2017) 20–30.
- [10] B. Xie, H. Yu, T. Sheng, Y. Xiong, Y. Ning, M.W. Fu, DDRX and CDRX of an as-cast nickel-based superalloy during hot compression at γ' sub-/super-solvus temperatures, *J. Alloys Compd.* 803 (2019) 16–29.
- [11] S.S.S. Kumar, T. Raghunath, P.P. Bhattacharjee, G.A. Rao, U. Borah, Evolution of microstructure and microtexture during hot deformation in an advanced P/M nickel base superalloy, *Mater. Charact.* 146 (2018) 217–236.
- [12] T. Konkova, S. Rahimi, S. Mironov, T.N. Baker, Effect of strain level on the evolution of microstructure in a recently developed AD730 nickel based superalloy during hot forging, *Mater. Charact.* 139 (2018) 437–445.
- [13] N.R. Jaladurgam, A.K. Kanjarla, Hot deformation characteristics and microstructure evolution of Hastelloy C-276, *Mater. Sci. Eng. A* 712 (2018) 240–254.
- [14] R.C. Buckingham, C. Argyrakakis, M.C. Hardy, S. Biroscica, The effect of strain distribution on microstructural developments during forging in a newly developed nickel base superalloy, *Mater. Sci. Eng. A* 654 (2016) 317–328.
- [15] K. Huang, K. Zhang, K. Marthinsen, R.E. Logé, Controlling grain structure and texture in Al-Mn from the competition between precipitation and recrystallization, *Acta Mater.* 141 (2017) 360–373.
- [16] Z.R. Zeng, Y.M. Zhu, S.W. Xu, M.Z. Bian, C.H.J. Davies, N. Birbilis, J.F. Nie, Texture evolution during static recrystallization of cold-rolled magnesium alloys, *Acta Mater.* 105 (2016) 479–494.
- [17] F. Shen, Z. Zhou, W. Li, Z. Sun, J. Tian, C. Xie, J. Guo, Z. Liao, D. Yi, J. Zhang, H. Wang, B. Jiang, Micro-mechanism of texture evolution during isochronal annealing of as-annealed hot rolled Al-Cu-Mg sheet, *Mater. Des.* 165 (2019), 107575.
- [18] Q. Zhao, Z. Liu, T. Huang, P. Xia, F. Li, Enhanced fracture toughness in an annealed Al-Cu-Mg alloy by increasing Goss/Brass texture ratio, *Mater. Charact.* 119 (2016) 47–54.
- [19] S.P. Coryell, K.O. Findley, M.C. Mataya, E. Brown, Evolution of microstructure and texture during hot compression of a Ni-Fe-Cr superalloy, *Metall. Mater. Trans. A* 43 (2012) 633–649.
- [20] Y. Wu, H. Kou, Z. Wu, B. Tang, J. Li, Dynamic recrystallization and texture evolution of Ti-22Al-25Nb alloy during plane-strain compression, *J. Alloys Compd.* 749 (2018) 844–852.
- [21] A.M. Kliauga, R.E. Bolmaro, M. Ferrante, The evolution of texture in an equal channel pressed aluminum AA1050, *Mater. Sci. Eng. A* 623 (2015) 22–31.
- [22] Q. Zang, H. Yu, Y.S. Lee, M.S. Kim, H.W. Kim, Hot deformation behavior and microstructure evolution of annealed Al-7.9Zn-2.7Mg-2.0Cu (wt%) alloy, *J. Alloys Compd.* 763 (2018) 25–33.
- [23] F.J. Humphreys, M. Hatherly, *Recrystallization and Related Annealing Phenomena*, 2nd ed. Elsevier, Oxford, 2004.
- [24] R. Madhavan, R.K. Ray, S. Suwas, New insights into the development of microstructure and deformation texture in nickel-60 wt.% cobalt alloy, *Acta Mater.* 78 (2014) 222–235.
- [25] X. Wang, B. Shen, L. Deng, J. Li, Effects of original orientation combination on substructure characteristics during continuous dynamic recrystallization in an extruded Al-Cu-Li alloy, *Mater. Charact.* 130 (2017) 113–122.
- [26] A.S. Taylor, P. Cizek, P.D. Hodgson, Orientation dependence of the substructure characteristics in a Ni-30Fe austenitic model alloy deformed in hot plane strain compression, *Acta Mater.* 60 (2012) 1548–1569.
- [27] H. Beladi, P. Cizek, P.D. Hodgson, Texture and substructure characteristics of dynamic recrystallization in a Ni-30%Fe austenitic model alloy, *Scr. Mater.* 61 (2009) 528–531.

- [28] Y.C. Lin, X.Y. Wu, X.M. Chen, J. Chen, D.X. Wen, J.L. Zhang, L.T. Li, EBSD study of a hot deformed nickel-based superalloy, *J. Alloys Compd.* 640 (2015) 101–113.
- [29] A.M. Wusatowska-Sarnek, H. Miura, T. Sakai, Nucleation and microtexture development under dynamic recrystallization of copper, *Mater. Sci. Eng. A* 323 (2002) 177–186.
- [30] R.R. Eleti, T. Bhattacharjee, A. Shibata, N. Tsuji, Unique deformation behavior and microstructure evolution in high temperature processing of HfNbTaTiZr refractory high entropy alloy, *Acta Mater.* 171 (2019) 132–145.
- [31] M. Hasegawa, M. Yamamoto, H. Fukutomi, Formation mechanism of texture during dynamic recrystallization in γ -TiAl, nickel and copper examined by microstructure observation and grain boundary analysis based on local orientation measurements, *Acta Mater.* 51 (2003) 3939–3950.
- [32] M. Rezayat, M.H. Parsa, H. Mirzadeh, J.M. Cabrera, Texture development during hot deformation of Al/Mg alloy reinforced with ceramic particles, *J. Alloys Compd.* 798 (2019) 267–272.
- [33] O. Engler, V. Randle, *Introduction to Texture Analysis: Macrotecture, Microtexture and Orientation Mapping*, 2nd ed. CRC Press, New York, 2010.
- [34] J. McCarley, S. Tin, Understanding the effects of recrystallization and strain induced boundary migration on $\Sigma 3$ twin boundary formation in Ni-base superalloys during iterative sub-solvus annealing, *Mater. Sci. Eng. A* 740–741 (2019) 427–438.
- [35] N. Dudova, A. Belyakov, T. Sakai, R. Kaibyshev, Dynamic recrystallization mechanisms operating in a Ni-20%Cr alloy under hot-to-warm working, *Acta Mater.* 58 (2010) 3624–3632.
- [36] H. Zhang, K. Zhang, H. Zhou, Z. Lu, C. Zhao, X. Yang, Effect of strain rate on microstructure evolution of a nickel-based superalloy during hot deformation, *Mater. Des.* 80 (2015) 51–62.
- [37] D. Jia, W. Sun, D. Xu, L. Yu, X. Xin, W. Zhang, F. Qi, Abnormal dynamic recrystallization behavior of a nickel based superalloy during hot deformation, *J. Alloys Compd.* 787 (2019) 196–205.
- [38] P.P. Bhattacharjee, G.D. Sathiaraj, M. Zaid, J.R. Gatti, C. Lee, C.W. Tsai, J.W. Yeh, Microstructure and texture evolution during annealing of equiatomic CoCrFeMnNi high-entropy alloy, *J. Alloys Compd.* 587 (2014) 544–552.
- [39] C. Haase, L.A. Barrales-Mora, D.A. Molodov, G. Gottstein, Texture evolution of a cold-rolled Fe-28Mn-0.28C TWIP steel during recrystallization, *Mater. Sci. Forum* 753 (2013) 213–216.
- [40] A. Guria, G.K. Mandal, P. Hodgson, J.H. Beynon, S.G. Chowdhury, Effect of twinning on microstructural evolution during dynamic recrystallisation of hot deformed as-cast austenitic stainless steel, *Metall. Mater. Trans. A* 46 (2015) 4423–4428.
- [41] M.L. Lobanov, S.V. Danilov, V.I. Pastukhov, S.A. Averin, Y.Y. Khrunyk, A.A. Popov, The crystallographic relationship of molybdenum textures after hot rolling and recrystallization, *Mater. Des.* 109 (2016) 251–255.
- [42] R.R. Eleti, T. Bhattacharjee, L. Zhao, P.P. Bhattacharjee, N. Tsuji, Hot deformation behavior of CoCrFeMnNi FCC high entropy alloy, *Mater. Chem. Phys.* 210 (2018) 176–186.
- [43] S. Mahajan, C.S. Pande, M.A. Imam, B.B. Rath, Formation of annealing twins in f.c.c. crystals, *Acta Mater.* 45 (1997) 2633–2638.
- [44] K. Huang, R.E. Logé, A review of dynamic recrystallization phenomena in metallic materials, *Mater. Des.* 111 (2016) 548–574.